Coupled Lossy Transmission Line Characterization and Simulation

It has been shown that the frequency domain solution of the coupled lossy transmission line differential equations has a similar appearance to that of the single line. The frequency-dependent $n \times n$ characteristic admittance matrix \mathbf{Y}_0 and propagation matrix Γ can be obtained from network analyzer insertion loss data treating the coupled transmission lines as a 2n-port network. This paper develops a transient simulation technique for coupled lossy transmission lines based on frequency-dependent \mathbf{Y}_0 and Γ data. Simulation results agree very well with transient measurements.

Introduction

Transmission lines are used for signal propagation between digital circuits in computers. They may appear as metal lines on IC (integrated circuit) chips, printed wires on PC (printed circuit) boards, flat or coaxial cables between boards, frames, etc. They may also appear as telephone cables between a computer and its peripheral devices. All of these conductors have finite losses. In the above applications, we are mainly interested in signal transient responses. Occasionally, we also have a need to investigate frequency domain responses for stability studies. Note that the driving and receiving circuits involved may be passive or active, linear or nonlinear. The transmission lines are usually surrounded by inhomogeneous dielectric media. For long-distance connections between a computer and its peripheral devices, we have low data rates and slow signal voltage transitions. On the other hand, the interconnections on IC chips or PC boards will carry high data rates with fast signal voltage transitions. The close spacing between adjacent lines requires careful attention to signal crosstalk. Sometimes we may have to ensure that the receiving circuit switches on the first incidence of signals. Sometimes it may take the signal voltage several trips back and forth on the transmission lines to switch the receiving circuit. In short, we need a versatile coupled lossy transmission line model capable of simulating all possible conditions. Of course, we are still limited to quasi-TEM waves. This requires that the cross section be independent of position along the lines and that separations between signal wires and the reference conductor be small with respect to the wavelength of the signal.

The equivalent circuit associated with the method of characteristics has been used for transient analysis of a single lossless line [1], coupled lossless lines [2-5], and coupled resistive lines [6, 7]. These simulation techniques satisfy the above requirements except that the frequency-dependent losses have been neglected. In this paper we shall extend the method of characteristics to transient simulations of coupled lossy lines having frequency-dependent line parameters, including skin effect, proximity effect, dielectric loss, etc.

The frequency dependencies of transmission line characteristics due to skin effect [8] and proximity effect [9] are well-known phenomena. Experimental data are available for many two-conductor cables [10, 11]. Recently, a frequency domain characterization technique for multiconductor transmission lines was presented [12]. The short-circuit input admittance and open-circuit input impedance data were required. The data analysis was based on the complex matrix solution of the coupled transmission line differential equations [13–16]. In addition to the short-circuit input admittance and open-circuit input im-

Copyright 1981 by International Business Machines Corporation. Copying is permitted without payment of royalty provided that (1) each reproduction is done without alteration and (2) the *Journal* reference and IBM copyright notice are included on the first page. The title and abstract may be used without further permission in computer-based and other information-service systems. Permission to republish other excerpts should be obtained from the Editor.

pedance data, we also include the transimpedance data from the network analyzer insertion loss measurements. The frequency-dependent characteristic admittance, attenuation, and related line parameters can then be obtained. Note that this measurement and data analysis technique is applicable to the general (n+1)-conductor transmission line system.

With frequency-dependent line parameters, the transient simulation has two difficulties. First, the characteristic admittance matrix is frequency-dependent, causing frequency-dependent reflection coefficients at both sending and receiving ends. Second, the propagation matrix is also frequency-dependent, causing signal waveform attenuation and dispersion. In the overhead multiphase power transmission system, the frequency-dependent earth resistance is an important parameter [17]. Many papers have been published investigating power-on transients and line-fault transients [18-23]. The 2n-port network parameters for the (n + 1)-conductor transmission lines [13] were used in the studies with the inverse Fourier integral [18] or the convolution integral [19]. In order to save computer time in their convolution integral methods, two investigators [20, 21] used the method of characteristics but neglected the frequency dependence of the characteristic admittance matrix. In other words, the frequency-dependent reflection coefficients were not included. A recent paper used a finite Fourier cosine transformation of the spatial independent variable (instead of time) to derive a lumped model [22]. It supplemented the conventional ladder network approach [23].

Instead of using the inverse Fourier integral or the convolution integral technique, a wave shaping network [24] was synthesized to account for the frequency-dependent attenuation for a single line. S. P. Madyiwa [25] and F. Briglez [26] developed a rigorous technique in synthesizing the wave shaping network. A ratio of two polynomials in the complex s-plane was derived such that the magnitude of the ratio evaluated on the imaginary axis approximated the attenuation of the transmission line of given length throughout the frequency range of interest. A cascade of constant-resistance bridged-T networks was then synthesized for this polynomial ratio. In both papers, the frequency dependence of the characteristic impedance was neglected. Therefore, the technique is limited to the high-frequency application of the single lossy line.

In this paper we combine the following techniques: 1) the decoupled mode transformation, 2) the method of characteristics, and 3) the wave shaping polynomial ratios together with state variable solution instead of network synthesis. They are integrated together for transient simulation of the general case of (n + 1)-conductor coupled

lossy transmission lines. All the information needed is derived from the frequency-dependent line parameters (i.e., R, L, G, and C matrices), which can be measured or calculated. The simulation technique takes into account the frequency-dependent attenuation and dispersion of transmitted and coupled signals. It also includes the frequency-dependent reflection coefficients, which may be nonlinear if nonlinear terminations are used.

In order to verify the simulation method, subroutines compatible with ASTAP [27] were written to perform transient simulations. The input data were the frequency-dependent line parameters obtained from two- and three-conductor cable measurements. The simulation results presented later are in excellent agreement with actual transient measurements. This paper describes the development and implementation of a simulation method for coupled lossy transmission lines that satisfies all requirements for computer applications mentioned above.

Frequency domain formula for coupled lossy transmission lines

For the (n + 1)-conductor coupled lines, the differential equations in the frequency domain can be expressed as follows:

$$\frac{d}{dx}\mathbf{V} = -\mathbf{Z}\mathbf{I},\tag{1}$$

$$\frac{d}{dx}\mathbf{I} = -\mathbf{Y}\mathbf{V},\tag{2}$$

where V is the $n \times 1$ vector for line voltage with respect to the reference conductor. I is the $n \times 1$ vector for line current. $\mathbf{Z} = \mathbf{R} + j\omega \mathbf{L}$, $\mathbf{Y} = \mathbf{G} + j\omega \mathbf{C}$. \mathbf{R} , \mathbf{L} , \mathbf{G} , and \mathbf{C} are $n \times n$ real symmetric matrices, which may be functions of frequency, but independent of x.

The solution of the above differential equations has been presented in several publications [13-16], with some assumptions being implicitly or explicitly expressed. We shall first quote the solution and follow with assumptions made. When these assumptions cannot be met, the simulation methods and characterization techniques presented in this paper will fail. The solution is

$$\mathbf{V} = \exp(-\Gamma x)\mathbf{A} + \exp(\Gamma x)\mathbf{B}, \tag{3}$$

$$\mathbf{Y}_{0}^{-1}\mathbf{I} = \exp(-\Gamma x)\mathbf{A} - \exp(\Gamma x)\mathbf{B}, \tag{4}$$

where

$$\Gamma = (\mathbf{Z}\mathbf{Y})^{1/2} = \mathbf{P}\gamma\mathbf{P}^{-1}, \qquad (5)$$

$$\mathbf{Y}_{\mathbf{a}} = \mathbf{Z}^{-1} \mathbf{\Gamma} = \mathbf{Y} \mathbf{\Gamma}^{-1} . \tag{6}$$

P is the eigenvector matrix of Γ . It is also the eigenvector matrix of the ZY product. γ is the diagonal eigenvalue

matrix of Γ . From the properties of functions of matrices [28], we have

$$\exp(-\Gamma x) = \mathbf{P} \exp(-\gamma x)\mathbf{P}^{-1}. \tag{7}$$

In the solution the existence of the complex matrix square root $(ZY)^{1/2}$ is assumed. And it is implied that Y_0 is a complex symmetrical matrix. We state the general assumptions in Appendix A.

The (n + 1)-conductor transmission lines of length d can be treated as a 2n-port network, having n ports on the sending end and n ports on the receiving end. It can be proved [29] that

$$\begin{bmatrix} \mathbf{I}_{S} \\ \mathbf{I}_{R} \end{bmatrix} = \begin{bmatrix} \mathbf{Y}_{0} \coth \Gamma d & -\mathbf{Y}_{0} \operatorname{csch} \Gamma d \\ -\mathbf{Y}_{0} \operatorname{csch} \Gamma d & \mathbf{Y}_{0} \operatorname{coth} \Gamma d \end{bmatrix} \begin{bmatrix} \mathbf{V}_{S} \\ \mathbf{V}_{R} \end{bmatrix}. \tag{8}$$

In other words, we have the short-circuit admittance matrix of the 2n-port network as follows:

$$\mathbf{Y}_{2n} = \begin{bmatrix} \mathbf{Y}_{A} & \mathbf{Y}_{B} \\ \mathbf{Y}_{R} & \mathbf{Y}_{A} \end{bmatrix}, \tag{9}$$

 $\mathbf{Y}_{\Delta} = \mathbf{Y}_{0} \coth \Gamma d$

 $Y_{\rm B} = -Y_{\rm 0} \operatorname{csch} \Gamma d$

From the definition of function of matrices [28], one has

 $\coth \Gamma d = \mathbf{P}(\coth \gamma d)\mathbf{P}^{-1}.$

 $\operatorname{csch} \Gamma d = \mathbf{P}(\operatorname{csch} \gamma d)\mathbf{P}^{-1}.$

P is the eigenvector of Γ , also of **ZY**. And the open-circuit impedance matrix is

$$\mathbf{Z}_{2n} = \begin{bmatrix} \mathbf{Z}_{\mathbf{A}} & \mathbf{Z}_{\mathbf{B}} \\ \mathbf{Z}_{\mathbf{B}} & \mathbf{Z}_{\mathbf{A}} \end{bmatrix}, \tag{10}$$

where

 $\mathbf{Z}_{\Lambda} = (\coth \Gamma d) \mathbf{Y}_{0}^{-1}$

 $\mathbf{Z}_{\mathrm{B}} = (\operatorname{csch} \Gamma d) \mathbf{Y}_{\mathrm{o}}^{-1}$.

Frequency domain characterization

After establishing Y_{2n} and Z_{2n} matrices from the insertion loss measurements described in Appendix B, we can then use Eq. (9) and/or Eq. (10) to derive Y_0 and Γ matrices. Of several methods considered by us, the following two data analysis methods appear to give the best accuracy.

• Data analysis method 1

This method was used in Ref. [12]. It is to be used when the transmission line attenuation is small. Since this method involves only measured data at one end of the coupled lines, the accuracy decreases when the reflected signal is highly attenuated. This consideration is important in the calculation of attenuation. From Eqs. (9) and (10), we have

$$\mathbf{Z}_{\mathbf{A}}\mathbf{Y}_{\mathbf{A}} = (\coth \Gamma d)^2$$
,

$$(\tanh \Gamma d)^2 = (\mathbf{Z}_{\mathbf{A}} \mathbf{Y}_{\mathbf{A}})^{-1} = \mathbf{P} \mathbf{\Lambda}_{\mathbf{Z}_{\mathbf{A}} \mathbf{Y}_{\mathbf{A}}}^{-1} \mathbf{P}^{-1},$$

$$tanh \Gamma d = \mathbf{P} \Lambda_{\mathbf{Z}_{A} \mathbf{Y}_{A}}^{-1/2} \mathbf{P}^{-1}, \tag{11}$$

$$\Gamma d = \mathbf{P} [tanh^{-1} \Lambda_{\mathbf{Z}_{A} \mathbf{Y}_{A}}^{-1/2}] \mathbf{P}^{-1}. \tag{12}$$

$$\Gamma d = \mathbf{P}[\tanh^{-1} \Lambda_{\mathbf{Z},\mathbf{Y}}^{-1/2}]\mathbf{P}^{-1}. \tag{12}$$

Note that P is the eigenvector matrix of $\mathbf{Z}_{A}\mathbf{Y}_{A}$ (and also of Γ matrix). From Eqs. (A2) and (12), we have

$$\gamma d = \tanh^{-1} \Lambda_{z,y}^{-1/2} . \tag{13}$$

Note that each diagonal element of the $\Lambda_{Z_1Y_1}^{-1}$ matrix has two roots, which are 180° out of phase. The proper one to use is the one with the positive real part, which will produce a positive real part for γd in Eq. (13). This can be proved through algebraic manipulation of $tanh \gamma d$ with complex argument yd. Each diagonal element in the diagonal matrix γd of Eq. (13) gives a propagation eigenvalue (attenuation and phase shift) for each decoupled mode. From Eqs. (9) and (11), we have

$$\mathbf{Y}_0 = \mathbf{Y}_{\mathbf{A}} \tanh \Gamma d = \mathbf{Y}_{\mathbf{A}} \mathbf{P} \Lambda_{\mathbf{Z}_{\mathbf{A}} \mathbf{Y}_{\mathbf{A}}}^{-1/2} \mathbf{P}^{-1}. \tag{14}$$

◆ Data analysis method 2

This method is to be used for transmission lines with high attenuation. This may happen either because the line is sufficiently long, or because the frequency of interest is so high that losses due to skin effect and proximity effect are significant. It involves the measurements at both sending and receiving ends of the coupled lines. From Eq. (9), we

$$-\mathbf{Y}_{\mathrm{B}}^{-1}\mathbf{Y}_{\mathrm{A}} = \cosh \Gamma d,$$

$$\Gamma d = \mathbf{P}[\cosh^{-1} \Lambda_{-\mathbf{Y}_{\mathrm{a}}^{-1}\mathbf{Y}_{\mathrm{A}}}]\mathbf{P}^{-1},$$
(15)

where **P** is the eigenvector matrix of $-\mathbf{Y}_{R}^{-1}\mathbf{Y}_{A}$. It is also the eigenvector matrix of Γd .

From Eqs. (A2) and (15), we have

$$\gamma d = \cosh^{-1} \left(\Lambda_{-\mathbf{Y}_{0}^{-1}\mathbf{Y}_{0}} \right). \tag{16}$$

From Eqs. (9) and (15), we have

 $Y_0 = -Y_B \sinh \Gamma d$

$$= -Y_B P[\sinh (\cosh^{-1} \Lambda_{-Y_B^{-1}Y_A})] P^{-1}.$$
 (17)

From Eq. (13) or (16), we can obtain for each decoupled mode the attenuation constant and the delay per unit length by dividing the real and the imaginary parts by d and ωd , respectively.

Having derived Γd [Eq. (12) or (15)], and \mathbf{Y}_0 [Eq. (14) or (17)], we can use Eq. (6) for the following:

$$\mathbf{Z} = \mathbf{R} + j\omega \mathbf{L} = \mathbf{\Gamma} \mathbf{Y}_{0}^{-1}, \tag{18}$$

$$\mathbf{Y} = \mathbf{G} + j\omega \mathbf{C} = \mathbf{Y}_{o} \mathbf{\Gamma}. \tag{19}$$

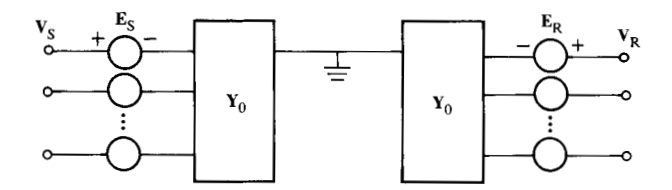


Figure 1 Coupled transmission line equivalent circuit.

Transient simulation technique

Before getting into the method used for lossy line transient simulation, we shall show that the equivalent circuit of Fig. 1 is applicable not only for simulation of ideal lines [2-5] but also for lossy lines if the following two conditions can be met:

- 1. The frequency-dependent characteristic admittance matrix \mathbf{Y}_0 can be simulated in time domain.
- 2. The proper relationship to express the E sources in terms of time and the terminal voltage exists.

The first of these conditions will be demonstrated later. We shall first show that the second condition can be met. Note that Eqs. (3) and (4) can be rewritten as follows:

$$\mathbf{V}(x) = \mathbf{V}^{+}(x) + \mathbf{V}^{-}(x), \tag{20}$$

$$\mathbf{Y}_{0}^{-1}\mathbf{I}(x) = \mathbf{V}^{+}(x) - \mathbf{V}^{-}(x), \tag{21}$$

where $V^+(x) = \exp(-\Gamma x)A$ is the forward propagating wave and $V^-(x) = \exp(\Gamma x)B$ is the backward propagating wave.

Evaluating Eqs. (20) and (21) at the sending end (x = 0), we have

$$\mathbf{E}_{s} = \mathbf{V}(x=0) - \mathbf{Y}_{0}^{-1}\mathbf{I}(x=0) = 2\mathbf{V}_{0}^{-1}(x=0). \tag{22}$$

Similarly, at the receiving end,

$$\mathbf{E}_{R} = \mathbf{V}(x = d) + \mathbf{Y}_{0}^{-1}\mathbf{I}(x = d) = 2\mathbf{V}^{+}(x = d). \tag{23}$$

From the definition $V^{-}(x) = \exp(\Gamma x)B$, we have

$$\mathbf{V}^{-}(x=0) = \mathbf{B} = \exp(-\Gamma d)\mathbf{V}^{-}(x=d).$$
 (24)

Substituting this equality into Eq. (22), we have

$$\mathbf{E}_{S} = 2 \exp(-\Gamma d)\mathbf{V}^{-}(x = d). \tag{25}$$

Evaluating Eq. (20) at the receiving end (x = d) and using Eq. (23), we have

$$\mathbf{V}^{-}(x = d) = \mathbf{V}(x = d) - \mathbf{V}^{+}(x = d) = \mathbf{V}_{R} - \frac{1}{2} \mathbf{E}_{R},$$
 (26)

where $V_R = V(x = d)$.

Combining Eqs. (25), (26), and (7) we have

$$\mathbf{E}_{S} = \mathbf{P}[\exp(-\gamma d)]\mathbf{P}^{-1}[2\mathbf{V}_{R} - \mathbf{E}_{R}]. \tag{27}$$

By symmetry, we have

$$\mathbf{E}_{R} = \mathbf{P}[\exp(-\gamma d)]\mathbf{P}^{-1}[2\mathbf{V}_{S} - \mathbf{E}_{S}], \tag{28}$$

where $V_s = V(x = 0)$.

This confirms the validity of the equivalent circuit of Fig. 1 for use with coupled lossy lines, as long as the operator $P[\exp{(-\gamma d)}]P^{-1}$, which in general is frequency-dependent, can be implemented in the time domain.

Equations (27) and (28) are true at any frequency. For the general case of lossy lines, elements of \mathbf{P} , \mathbf{P}^{-1} , and $\exp(-\gamma d)$ matrices are functions of frequency. We can approximate each element in the \mathbf{P} and \mathbf{P}^{-1} matrices as a ratio of two polynomials in the complex s-plane. The poles and zeros of this ratio are placed on the real axis. The ratio is to be evaluated on the imaginary axis. The locations of poles and zeros are adjusted to give a good approximation to this ratio in both magnitude and phase throughout the frequency range of interest.

Note that $\exp(-\gamma d)$ is a diagonal matrix. We shall first factor out for each diagonal element the corresponding constant delay operator. This is

$$\exp(-\gamma_{\nu}d) \equiv A_{\nu} \exp(-j\beta_{\nu}d). \tag{29}$$

Note that β_k is the high-frequency asymptote of the imaginary part of γ_k .

Taking the absolute value of both sides of the above equation, we have

$$\exp\left(-\alpha_{\nu}d\right) = |A_{\nu}|. (30)$$

That is, the magnitude of A_k represents the attenuation of kth decoupled mode.

 A_k in Eq. (29) can then be approximated by a ratio of two polynomials in the complex s-plane as is an element in the **P** matrix discussed before. In the complex s-plane exp $(-j\beta_k d)$ can be rewritten as exp $(-s\tau_k d)$. Then, Eq. (19) becomes

$$\exp(-\gamma_{\nu}d) \cong A_{\nu}(s) \exp(-s\tau_{\nu}d). \tag{31}$$

Note that τ_k is the high-frequency limit of the kth-mode delay time.

We can now treat Eqs. (27) and (28) as the Laplace transforms relating $\mathbf{E}_{\mathrm{S}}(s)$ and $\mathbf{E}_{\mathrm{R}}(s)$ to $\mathbf{V}_{\mathrm{S}}(s)$ and $\mathbf{V}_{\mathrm{R}}(s)$. The triple-matrix product $\mathbf{P}[\exp{(-\gamma d)}]\mathbf{P}^{-1}$ can be treated as three operators in cascade.

The physical meaning of Eq. (28) can be expressed as follows:

- The incident wave (1/2)[2V_s E_s] is broken up into n decoupled modes as determined by the product (1/2)P⁻¹[2V_s E_s]. This product produces a vector M. Its kth component, M_k, represents the kth component of the decoupled wave.
- 2. Each component of the decoupled mode, M_k , is then operated on by the appropriate operator $\exp(-\gamma d)$, which is shown in Eq. (31). This results in a signal delay of $\tau_k d$, plus attenuation and dispersion represented by $A_k(s)$.
- 3. These modified mode magnitudes, properly lined up in time represented by the $\exp(-s\tau_k d)$ operator, form a new vector, which is then multiplied by **P** to yield the resultant voltage vector $\mathbf{E}_{\mathbf{R}}$. From Eq. (23), we note that $(1/2)\mathbf{E}_{\mathbf{R}}$ represents the incident voltage vector arriving at the receiving end.

Similar physical meaning also applies to \mathbf{E}_{S} in Eq. (27). Here $(1/2)[2\mathbf{V}_{\mathrm{R}}-\mathbf{E}_{\mathrm{R}}]$ represents the reflected voltage vector at the receiving end. From Eq. (22), we note that $(1/2)\mathbf{E}_{\mathrm{S}}$ represents the reflected voltage vector returning back to the sending end.

The implementation of the equivalent circuit in Fig. 1 in a circuit simulation program can be accomplished using the voltage-dependent current sources of Fig. 2. The Laplace transforms of these current sources \mathbf{J}_{S} and \mathbf{J}_{R} and the terminal voltages \mathbf{V}_{S} and \mathbf{V}_{R} are related by the following equations:

$$\mathbf{J}_{\mathbf{S}} = \mathbf{Y}_{\mathbf{0}}[\mathbf{V}_{\mathbf{S}} - \mathbf{E}_{\mathbf{S}}],\tag{32}$$

$$\mathbf{J}_{\mathbf{R}} = \mathbf{Y}_{\mathbf{0}}[\mathbf{V}_{\mathbf{R}} - \mathbf{E}_{\mathbf{R}}],\tag{33}$$

where

$$\mathbf{E}_{\mathbf{S}} \cong \mathbf{P} \mathbf{A}[\exp(-s\tau d)]\mathbf{P}^{-1}[2\mathbf{V}_{\mathbf{R}} - \mathbf{E}_{\mathbf{R}}], \tag{34}$$

$$\mathbf{E}_{\mathbf{R}} \cong \mathbf{P} \mathbf{A}[\exp(-s\tau d)]\mathbf{P}^{-1}[2\mathbf{V}_{\mathbf{S}} - \mathbf{E}_{\mathbf{S}}]. \tag{35}$$

(The \mathbf{E}_{S} and \mathbf{E}_{R} vectors represent intermediate state variables.)

• Single line transient simulation

For a single transmission line, P and P^{-1} in Eqs. (34) and (35) are scalars of unit magnitude. Therefore, Eq. (34) becomes

$$E_{\rm S}(s) \cong A(s)[\exp{(-s\tau d)}][2V_{\rm R}(s) - E_{\rm R}(s)]$$

$$= A(s)E_{\rm H}(s), \tag{36}$$

where

$$E_{11}(s) \equiv [\exp(-s\tau d)][2V_{R}(s) - E_{R}(s)],$$

or

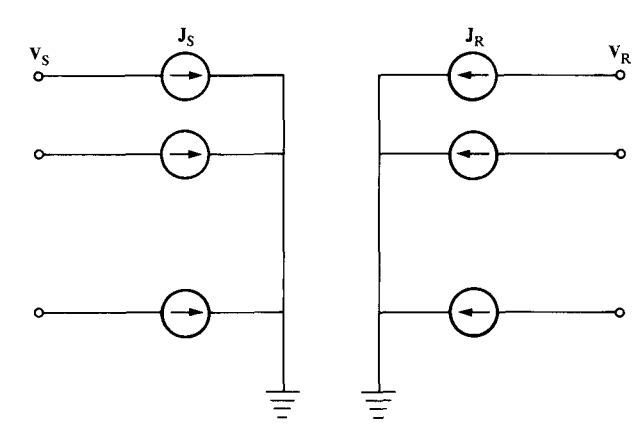


Figure 2 Current source representation for coupled transmission lines.

$$e_{tt}(t) = \mathcal{L}^{-1}[E_{tt}(s)] = 2v_{R}(t - \tau d) - e_{R}(t - \tau d).$$
 (37)

A(s) in Eq. (36) can be treated as a transfer function relating $E_{\rm S}(s)$ to $E_{\rm tr}(s)$. It is well known that a transfer function having the number of poles equal to or greater than the number of zeros can be simulated by means of state variables, using numerical integration [30, 31]. The only assumption that is needed is that the analytic expression represents a stable network. By restricting the poles to the left-half plane in the routine that produces a ratio of two polynomials to approximate A(s), this problem is avoided. From many simulation exercises we had done, it was found that those poles and zeros resulting in good approximation to the magnitude of A(s), which was equal to exp $(-\alpha d)$ as shown in Eq. (30), would also give a good approximation to the phase of A(s).

From Eq. (36), we have

$$\frac{E_{\rm S}(s)}{E_{\rm t1}(s)} = A(s) \cong \frac{a_{\rm m}s^{\rm m} + a_{\rm m-1}s^{\rm m-1} + \cdots + a_{\rm 1}s + a_{\rm 0}}{s^{\rm n} + b_{\rm n-1}s^{\rm n-1} + \cdots + b_{\rm 1}s + b_{\rm 0}} ,$$

 $m \leq n$.

$$E_{S}(s) \cong (a_{m}s^{m} + a_{m-1}s^{m-1} + \cdots + a_{1}s + a_{0})E_{n1}(s),$$
 (38)

where

$$E_{u1}(s) = \frac{1}{s^n + b_{n-1}s^{n-1} + \cdots + b_ns + b_0} E_{t1}(s),$$

or

$$E_{t1}(s) = (s^{n} + b_{n-1}s^{n-1} + \cdots + b_{1}s + b_{0})E_{u1}(s).$$
 (39)

Note that $E_{u_1}(s)$ is an intermediate state in Eqs. (38) and (39). Taking the inverse Laplace transform of Eq. (38), we have

29

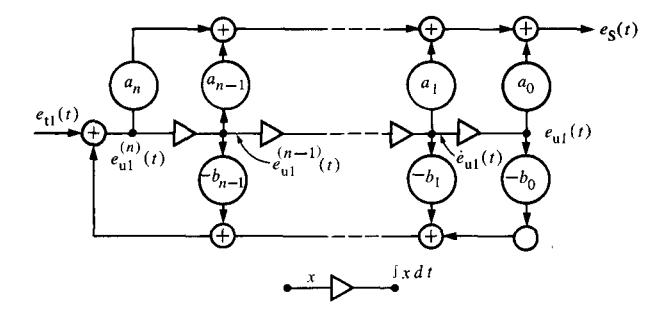


Figure 3 Transfer function implementation using state variables. The triangular box represents a time integrator.

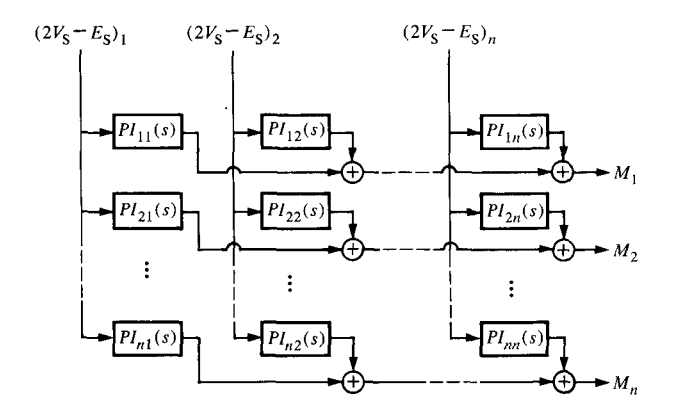


Figure 4 Derivation of decoupled mode voltage vector M.

$$e_{S}(t) \approx a_{m} e_{u1}^{(m)}(t) + a_{m-1} e_{u1}^{(m-1)}(t) + \cdots + a_{1} e_{u1}(t) + a_{0} e_{u1}(t), \tag{40}$$

where $e_{u1}^{(k)}(t)$ is the kth derivative of $e_{u1}(t)$.

Next, we have to express $e_{u1}(t)$ and its derivatives in terms of $e_{t1}(t)$, which is available from Eq. (37). From Eq. (39), we have

$$s^{n}E_{u1}(s) = E_{t1}(s) - (b_{n-1}s^{n-1} + \cdots + b_{1}s + b_{0})E_{u1}(s),$$

$$e^{(n)}_{u1}(t) = e_{t1}(t) - b_{n-1}e^{(n-1)}_{u1}(t) - \cdots - b_{1}\dot{e}_{u1}(t)$$

$$- b_{0}e_{u1}(t). \tag{41}$$

Once the highest derivative $e_{u1}^{(n)}(t)$ is known, the remaining lower-order derivatives of $e_{u1}(t)$ may be obtained by successive integrations. Equation (41) looks like a feedback loop with $e_{t1}(t)$ as its input, and $e_{u1}^{(n)}(t)$, $e_{u1}^{(n-1)}(t)$, \cdots , $e_{u1}(t)$, and $e_{u1}(t)$ as the outputs. The negative feedback coefficients are b_{n-1}, \cdots, b_1 , and b_0 . Equation (40) is then used to obtain $e_s(t)$. This is illustrated in Fig. 3 for m = n [32]. When implemented in a program the integrations are performed numerically.

Note that $\mathbf{Y}_0(s)$ in Eq. (32) can be regarded as a transfer function relating $\mathbf{J}_S(s)$ to $[\mathbf{V}_S(s) - \mathbf{E}_S(s)]$. We shall approximate $\mathbf{Y}_0(s)$ by a ratio of two polynomials having poles on the negative real axis. Having obtained a good approximation for $\mathbf{Y}_0(s)$, we can apply the numeric technique shown in Fig. 3. This time, the input is $[v_S(t) - e_S(t)]$, and the output is $j_S(t)$. Similar procedure also applies to Eq. (33) to obtain $j_P(t)$.

• Coupled line transient simulation

For the general case of coupled lossy line transient simulation, four different operators, \mathbf{P}^{-1} , \mathbf{A} , \mathbf{P} , and \mathbf{Y}_0 , are involved in the implementation of the equivalent circuit described in Fig. 2 and Eqs. (32) to (35). \mathbf{P}^{-1} , \mathbf{P} , and \mathbf{Y}_0 are $n \times n$ matrices, \mathbf{A} is an $n \times n$ diagonal matrix having n nonzero entries. The first operation to be performed is the breakup of the incident waves into the decoupled modes. This involves the operator \mathbf{P}^{-1} on the vector $[2\mathbf{V}_S - \mathbf{E}_S]$. We treat each entry of the \mathbf{P}^{-1} matrix as a transfer function. That is,

$$\mathbf{P}^{-1} \equiv \begin{bmatrix} (PI)_{11} & (PI)_{12} & (PI)_{1n} \\ \vdots & \vdots & \vdots \\ (PI)_{n1} & (PI)_{n2} & (PI)_{nn} \end{bmatrix}.$$

Here, each of the entries, PI_{jk} , will be approximated by a ratio of two polynomials, similar to $\mathbf{A}(s)$ and $\mathbf{Y}_0(s)$ in the previous section of single line transient simulation. The product $\mathbf{P}^{-1}[2\mathbf{V}_S - \mathbf{E}_S]$ is illustrated in Fig. 4.

Note that the $PI_{jk}(s)$ transfer functions do not represent a physical system in the same manner as $\mathbf{A}(s)$ and $\mathbf{Y}_0(s)$ do for the single line case. It is, therefore, possible that for a good polynomial approximation to $PI_{jk}(s)$, magnitude and phase, poles in the right-half plane may be required. Since this would result in an unstable network, it is not permitted. An accurate broad-band model for such structure is not possible. We have to limit the applicable frequency range such that the poles on the right-half plane can be neglected. We have analyzed many structures which have been used in the laboratories, including up to a five-conductor configuration. The poles for \mathbf{P}^{-1} and \mathbf{P} have always been on the left-half plane. For the case of two symmetrical lines, the eigenvectors are independent of frequency.

Once the decoupled mode voltage vector \mathbf{M} ($\mathbf{M} = \mathbf{P}^{-1}[2\mathbf{V}_{\mathrm{S}} - \mathbf{E}_{\mathrm{S}}]$) is established at each time step, each component of the \mathbf{M} vector is stored in a table for all time steps of interest. The data can then be extracted after a period of time equal to the delay for the corresponding decoupled mode. This procedure is identical to that used for delay simulation of coupled ideal lines [4]. Now we have a new voltage vector $\mathbf{N} = \exp(-s\tau d)\mathbf{P}^{-1}[2\mathbf{V}_{\mathrm{S}} - \mathbf{E}_{\mathrm{S}}]$.

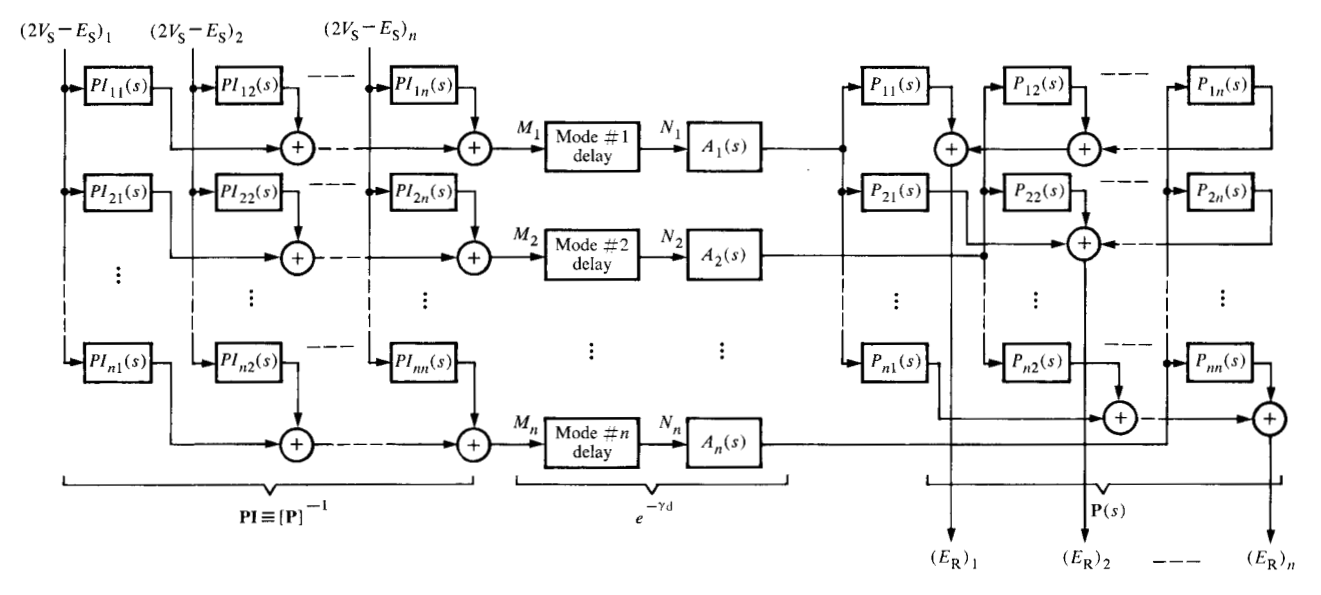


Figure 5 Block diagram indicating the operations involved in solution of voltage source vector E_R.

Each component of the N vector is then operated on by the corresponding component of the transfer function $\mathbf{A}(s)$, representing attenuation and dispersion for that particular decoupled mode. The resultant voltage vector is $\exp{(-\gamma d)}\mathbf{P}^{-1}\left[2\mathbf{V}_{\mathrm{S}}-\mathbf{E}_{\mathrm{S}}\right]$, representing twice the incident decoupled mode voltages at the receiving end. This voltage vector is then operated on by the operator \mathbf{P} . The result is the \mathbf{E}_{R} vector of Eq. (35). The overall operation is illustrated in Fig. 5. The \mathbf{E}_{S} vector of Eq. (34) can be obtained in a similar procedure. Note the effect of the delay operator $\exp{(-s\tau d)}$ in Eqs. (34) and (35). The \mathbf{E}_{S} and \mathbf{E}_{R} vectors on the left-hand side are constructed from earlier values of those on the right-hand side.

The \mathbf{Y}_0 matrix in Eqs. (32) and (33) has $n \times n$ entries. It has been shown to be symmetrical. If we implement Eq. (32) as shown, we have to perform all n^2 operations without taking advantage of the symmetry of \mathbf{Y}_0 . Note that the kth component of the \mathbf{J}_S vector of Eq. (32) can be expressed as follows:

$$(\mathbf{J}_{S})_{k} = (\mathbf{Y}_{0})_{k1}(\mathbf{V}_{S} - \mathbf{E}_{S})_{1} + \cdots + (\mathbf{Y}_{0})_{kk}(\mathbf{V}_{S} - \mathbf{E}_{S})_{k}$$

$$+ \cdots + (\mathbf{Y}_{p})_{kn}(\mathbf{V}_{S} - \mathbf{E}_{S})_{n}$$

$$= \left[\sum_{j=1}^{n} (\mathbf{Y}_{0})_{kj}\right] (\mathbf{V}_{S} - \mathbf{E}_{S})_{k}$$

$$+ \sum_{j \neq k} (-\mathbf{Y}_{0})_{kj}[(\mathbf{V}_{S} - \mathbf{E}_{S})_{k} - (\mathbf{V}_{S} - \mathbf{E}_{S})_{j}]. \tag{42}$$

There are (n-1) terms represented by the summation on the right-hand side of Eq. (42); the kj-term in this equation is the negative of the jk-term of the $(\mathbf{J}_S)_j$ component. We can take advantage of this relation and implement Eq. (42) with n(n+1)/2 operations. Here, we shall treat $\sum_{j=1}^{n} (\mathbf{Y}_0)_{kj}$ and $(-\mathbf{Y}_0)_{kj}$ as the transfer functions, relating the kth component of \mathbf{J}_S to the vector $(\mathbf{V}_S - \mathbf{E}_S)$. Each of the transfer functions is to be approximated by a ratio of two polynomials, having poles on the negative real axis. The inverse Laplace transform of Eq. (42) will result in $[i_S(t)]_k$. Extending this operation to all components in \mathbf{J}_S and \mathbf{J}_R of Eqs. (32) and (33), we derive the 2n current sources shown in Fig. 2. Each of these 2n current sources depends on the 2n terminal voltages shown as the \mathbf{V}_S and \mathbf{V}_R vectors.

Experimental results

In the previous two sections, we have explained the characterization of lossy transmission lines to derive the characteristic admittance matrix \mathbf{Y}_0 and the propagation matrix Γ . We have also explained transient simulation routines. In this section, we shall exercise the measurement technique presented in this paper and demonstrate the validity of the transient simulation method. We shall confine the experiments to the low-frequency range (say below 1 MHz) to minimize the effect of discontinuities due to line connections. For this reason, we use a commercial telecommunication cable. It consists of four AWG22 con-

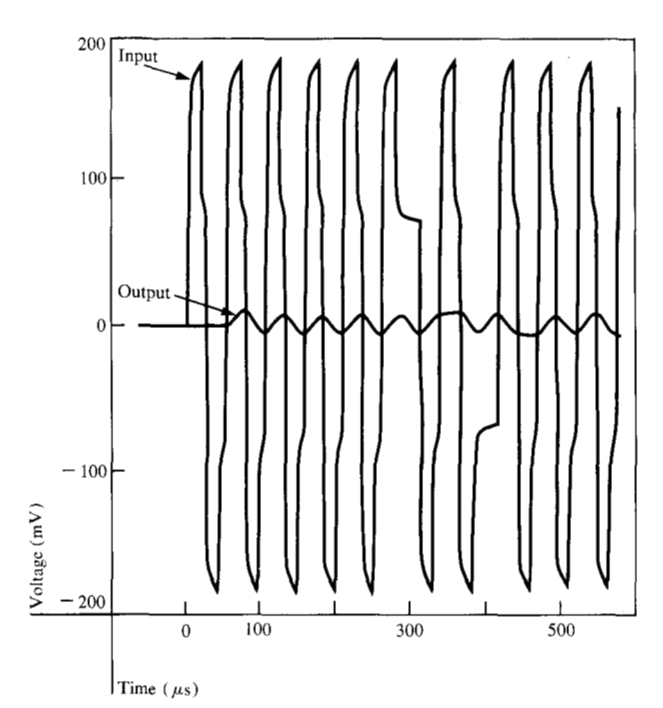


Figure 6 Input waveform and simulated transient response for 8.98-km cable.

Table 1 Insertion loss data for 1344-meter cable.

Freq. (kHz)	Y ₁₁ connection		2-port connection		Z_{11} connection	
	(dB)	(deg.)	(dB)	(deg.)	(dB)	(deg.)
0.1	-7.72	-0.29	-7.22	-7.43	-47.24	88.36
0.2	-7.71	-0.35	-7.56	-4.86	-42.95	89.58
0.5	-7.72	-0.61	-7.68	-3.24	-34.75	88.51
1	-7.72	-1.01	-7.7	-3.7	-28.64	86.87
2	-7.74	-1.87	-7.7	-5.89	-22.66	83.71
5	-7.9	-4.41	-7.71	-13.62	-14.66	73.99
10	-8.47	-7.78	-7.74	-26.65	-9.16	58.48
20	-10.58	-6.71	-7.76	-52.25	-5.15	30.63
50	-5.99	23.89	-6.99	-134.2	-8.22	-10.79
100	-9.12	10.14	-8.99	87.91	~5.49	1.43
200	-6.1	3.47	-12.09	-170.5	-7.74	2.33
500	-6.54	0.93	-20.1	155.7	-6.78	1.66

ductors in two color-coded twisted pairs. They are wrapped around by aluminum-coated mylar and a braided shield. For the single line measurements, we use the blue pair to carry the signal and return current. The orange pair is tied together with the shield and left floating. For the two coupled lines (3-conductor configuration) measurements, we used the solid blue and the blue stripe

wires as signal-carrying conductors. The orange pair and the shield were tied together for the return current conductor.

• Single line comparisons

The insertion loss measurements were made on the blue pair of the 1344-meter cable using the HP3042A network analyzer from 100 Hz to 500 kHz. The measured data are shown in Table 1. Using the frequency domain characterization technique discussed in this paper, we derived the transmission line parameters shown in Table 2. The 1344-meter cable represents one wavelength at about 135 kHz. The accuracy of the derived phase shift and delay time at f < 5 kHz is questionable. Note that $\omega L \equiv R$ at 25 kHz; therefore, the accuracy of the derived line resistance value at f > 400 kHz is also questionable. These parameters have been blocked out in Table 2. Note that the shunt conductance is not shown in Table 2 because it was negligibly small so that the derived values were in the noise range.

In establishing the ratios of polynomials for $\mathbf{A}(s)$ and $\mathbf{Y}_0(s)$, we have concentrated on their magnitudes. The resultant polynomial ratio approximates the phase angle quite well too. Note that $\mathbf{Y}_0(s)$ is independent of line length. But $\mathbf{A}(s)$ is an exponential function of line length, as shown in Eq. (30). Subroutines to establish the polynomial ratios and to convert them for numerical integration, shown in Fig. 3, have been written. They are compatible with ASTAP [27].

An ASTAP run [32] has been set up to simulate an 8.96-km line with 155 ohms plus $0.02~\mu F$ shunt capacitance load. The line is driven by a 19.2-kb/s biphase, predistorted signal with 370 mV peak-to-peak amplitude [7]. The simulated ASTAP plot is shown in Fig. 6. Note that the output signal waveform is drastically distorted and attenuated to 16 mV peak-to-peak voltage, which represents a factor of 23 attenuation.

Additional ASTAP runs [32] were arranged to produce the "eye patterns" [33] for two different line lengths, 6.45 km and 8.96 km, for comparison with the transient measurements, as shown in Fig. 7. The simulated eye patterns have a peak-to-peak magnitude of 33 mV for 6.45-km line and 16 mV for 8.96-km line. They are somewhat higher than the measured values of 31 mV and 13.5 mV, respectively. These discrepancies are within the measurement accuracy of the line length, the insertion loss, the oscilloscope, etc. Note that the shapes of the eye patterns, including the detailed bends and corners, agree very well with the measured results.

Table 2 Cable parameters derived from measurements.

Freq. (kHz)		$\mathbf{Z_{o}}$						
	(dB/m)	(Ω)	(deg.)	(Lambda)	(ns/m)	(Ω/m)	(nH/m)	(pF/m)
0.1	-0.0003069	1815.44	-44.06			0.1005		48.70
0.2	-0.0004201	1416.86	-44.70			0.1044		41.41
0.5	-0.0007062	884.50	-44.26			0.1060		43.17
1	-0.001009	621.95	-43.64			0.1062		43.77
2	-0.001405	440.88	-42.38			0.1062	840.3	43.68
5	-0.002115	278.73	-38.61	0.07	9.743	0.1063	773.7	44.67
10	-0.002711	204.02	-33.00	0.10	7.653	0.1068	757.6	44.72
20	-0.003229	160.44	-24.68	0.17	6.505	0.1090	750.2	44.54
50	-0.003964	135.98	-13.49	0.40	5.942	0.1196	739.6	44.98
100	-0.004997	128.83	-9.28	0.77	5.731	0.1480	709.7	45.05
200	-0.007870	121.28	-5.41	1.48	5.512	0.1885	657.2	45.80
500	-0.01384	115.31	-2.41	3.57	5.311		609.4	46.20

Table 3 Four-port network insertion loss data: (a) short-circuit (above), (b) open-circuit (below).

Freq. (kHz)	a^{s}	SC 11	a	SC 12	a	SC 13	·	I ^{SC} 14
	(dB)	(deg.)	(dB)	(deg.)	(dB)	(deg.)	(dB)	(deg.)
0.1	-5.26	-0.20	-22.34	0.22	5.26	-0.76	-22.40	-172.68
0.2	-5.27	-0.26	-22.35	0.35	-5.27	-0.81	-22.39	-177.32
0.5	-5.26	-0.51	-22.34	0.79	-5.25	-1.54	-22.36	-178.99
1	-5.27	-0.90	-22.31	1.39	-5.26	-2.91	-22.33	-1.24
2	-5.29	-1.65	-22.25	2.58	-5.25	-5.69	-22.26	178.83
5	-5.41	-3.91	-21.84	4.98	-5.26	-14.11	-21.76	176.02
10	-5.92	-6.90	-21.07	3.92	-5.29	-28.01	-20.57	166.38
20	-7.73	-5.66	-21.46	-4.13	-5.36	-55.44	-18.77	136.33
50	-3.94	17.75	-19.23	11.56	-5.67	-139.70	-18.81	32.73
100	-6.35	7.79	-22.28	13.07	-7.55	86.90	-19.67	-98.61
200	-4.19	3.22	-19.72	-6.19	-11.01	-166.11	-23.25	-10.37
500	-4.42	1.67	-21.05	-6.43	-19.22	173.86	-28.90	-50.81
1000	-4.40	0.34	-21.02	0.60	-28.34	78.05	-32.70	-146.04
Freq. (kHz)	a	OC 11	a ^c	DC 12	а	OC 13	C	10C 14
(KIIZ)	(dB)	(deg.)	(dB)	(deg.)	(dB)	(deg.)	(dB)	(deg.)
0.1	-43.05	88.39	-56.66	88.54	-5.36	-0.84	-57.10	89.34
0.2	-38.69	89.31	-52.66	89.11	-5.36	-0.85	-52.64	88.96
0.5	-30.53	87.84	-44.65	87.85	-5.36	-1.55	-44.65	87.11
1	-24.47	85.58	-38.59	85.47	-5.36	-2.93	-38.57	84.11
2	-18.44	81.13	-32.51	80.67	-5.36	-5.71	-32.46	77.94
5	-10.79	68.03	-24.72	66.53	-5.38	-14.17	-24.43	59.34
10	-5.97	49.25	-19.88	44.31	-5.42	-28.09	-18.69	27.86
20	-3.32	22.66	-18.34	12.33	-5.51	-55.47	-14.73	-35.63
50	-5.86	-7.48	-21.30	-14.87	-5.81	-139.31	-22.53	-168.78
100	-3.90	2.08	-18.93	-8.38	-7.74	87.56	-21.22	86.15
200	-5.39	1.45	-22.37	8.33	-11.20	-163.95	-27.60	-128.44
500	-4.70	1.88	-21.45	1.25	-19.37	-144.93	-30.75	-114.64
1000	-4.50	0.35	-21.00	-1.15	-28.81	88.81	-34.49	154.48

• Coupled line comparisons

When the two blue-colored conductors in the 1344-meter cable were treated as two coupled lines, we had a four-port network. The short-circuit and open-circuit insertion

loss measurement results are shown in Tables 3(a) and (b). The coupled line characteristic admittance matrix \mathbf{Y}_0 has been derived from these data. Table 4(a) shows the frequency-dependent Y_{10} , Y_{20} , and $-Y_{12}$. Here we have

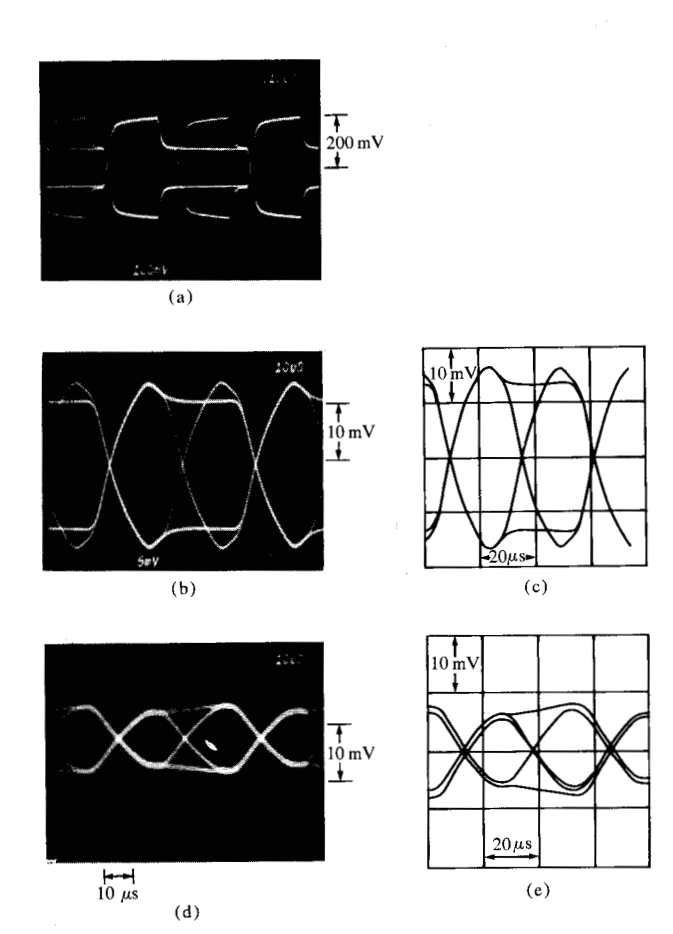


Figure 7 Comparison of simulated and measured eye patterns. (a) Measured input waveform (also used as simulation input). (b) Measured response of 6.45-km cable. (c) Predicted response of 6.45-km cable. (d) Measured response of 8.96-km cable. (e) Predicted response of 8.96-km cable. Note that for all cases line is terminated in 155 $\Omega \parallel 0.02~\mu F$.

defined $Y_{10} = (\mathbf{Y}_0)_{11} + (\mathbf{Y}_0)_{12}$, and $Y_{20} = (\mathbf{Y}_0)_{22} + (\mathbf{Y}_0)_{21}$. In Table 4(b), we show the derived exp $(-\Gamma d)$ in an indirect way, as explained below.

1. The eigenvector matrix \mathbf{P} for the propagation matrix $\mathbf{\Gamma}$ for the two symmetrical coupled lines is

$$\mathbf{P} = \frac{1}{\sqrt{2}} \begin{vmatrix} 1 & 1 \\ -1 & 1 \end{vmatrix}$$
 at all frequencies.

- 2. Attenuation $\equiv (20 \log_{10} |\exp(-\gamma d)|)/\text{line length}$.
- 3. Delay \equiv Imaginary part of exp $(-\gamma d)/\omega \times$ line length.
- 4. Mode 1 is the difference mode, and Mode 2 is the common mode as defined by the P matrix above.

The frequency-dependent R, L, and C matrices were derived from the Y_0 and Γ matrices. They are shown in

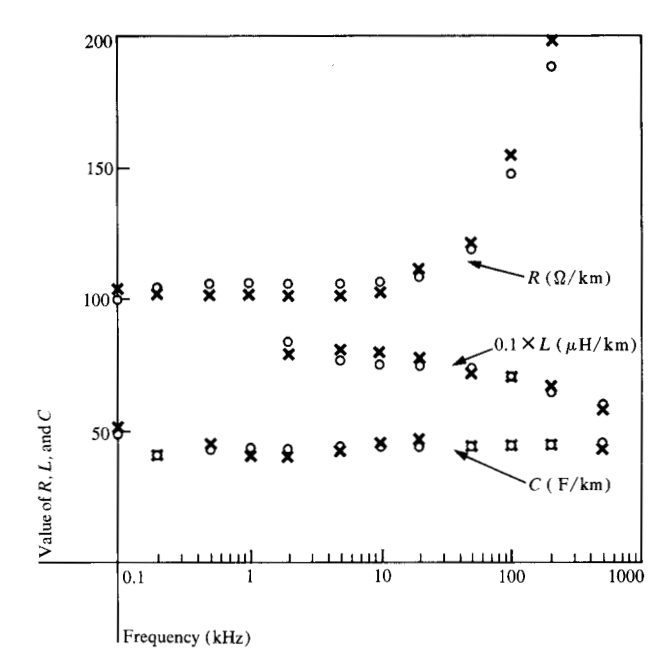


Figure 8 Twisted pair line parameters: ○—single twisted pair; ×—the difference mode of two coupled lines.

Table 5. Several entries in Tables 4(b) and 5 have been blocked out for the same reasons as applied to Table 2. Note that the difference mode of the two coupled lines is equivalent to the single twisted pair discussed earlier in this section. The $R_{\rm D}$, $L_{\rm D}$, and $C_{\rm D}$ parameters of the difference mode can be proved to be

$$R_{\rm D} = 2 \times (R_{11} - R_{12}),$$

$$L_{\rm D} = 2 \times (L_{11} - L_{12}),$$

$$C_{\rm D} = 0.5 \times (C_{11} - C_{12}).$$

The comparisons of these parameters with the R, L, and C parameters of the single twisted pair are shown in Fig. 8. The line capacitance is independent of frequency. The line inductance decreases at high frequencies, as is expected due to the decrease of the internal inductance contribution. The differences between C and L of the difference mode of two coupled lines and those of the single twisted pair are within the measurement accuracy. The difference for the line series resistance at $f \le 50 \text{ kHz}$ is negligible. At f = 100 kHz and 200 kHz, the differences are 5% and 6%, respectively, which could be due to measurement errors. Further investigation is necessary. The comparison of the magnitude of the attenuation is shown in Fig. 9. The differences are very small. Also shown in Fig. 9 is the comparison of the magnitudes of the characteristic impedances. For the difference mode, we have

Table 4 Coupled transmission line characteristics: (a) admittances (above), (b) attenuation and delay (below).

Admittance Freq. (kHz)	Y_{10}		Y_{20}		Y_{12}	
	Mag (mS)	Phase (deg.)	Mag (mS)	Phase (deg.)	Mag (mS)	Phase (deg.)
0.1	0.77	44.13	0.77	44.13	0.17	-135.58
0.2	0.99	44.67	0.99	44.67	0.21	-135.17
0.5	1.59	44.10	1.59	44.10	0.34	-135.26
1	2.25	43.33	2.25	43.33	0.48	-135.61
2	3.18	41.86	3.18	41.86	0.69	-136.28
5	4.98	37.43	4.98	37.43	1.10	-138.55
10	6.68	31.46	6.68	31.46	1.57	-143.25
20	8.27	23.84	8.27	23.84	2.11	-153.53
50	10.02	14.70	10.02	14.70	2.33	-168.86
100	10.42	10.31	10.42	10.31	2.57	-171.64
200	11.30	6.16	11.30	6.16	2.52	-174.80
500	12.11	5.06	12.11	5.06	2.58	-178.97
1000	12.45	0.85	12.45	0.85	2.75	-179.66

Freq. (kHz)	Attenuatio	on (dB/km)	Delay (μs/km)		
(KIIZ)	Mode 1	Mode 2	Mode 1	Mode 2	
0.1	0.35	0.36			
0.2	0.45	0.46			
0.5	0.71	0.73			
1	0.99	1.03			
2	1.38	1.43			
5	2.03	2.12	9.61	9.69	
10	2.59	2.71	7.74	7.65	
20	3.24	3.28	6.65	6.50	
50	4.02	4.32	5.93	5.93	
100	5.33	5.88	5.75	5.67	
200	8.01	8.59	5.55	5.44	
500	13.60	14.29	5.25	5.14	
1000	19.44	21.94	5.08	4.97	

$$(\mathbf{Z}_{0})_{D} = 1/(\mathbf{Y}_{0})_{D},$$

 $(\mathbf{Y}_{0})_{D} = 0.5 \times [(\mathbf{Y}_{0})_{11} - (\mathbf{Y}_{0})_{12}] = 0.5 \times (\mathbf{Y}_{0})_{10} - (\mathbf{Y}_{0})_{12}.$
Here we have an excellent agreement.

From Table 4(b) we note that the high-frequency limit of the delay time of the common mode (Mode 2) is smaller than that of the difference mode (Mode 1). It can be explained as follows: Note that the difference mode energy travels in the dielectric between the two conductors of the blue twisted pair. The common mode energy travels in the dielectric between the blue pair as one conductor, and the orange pair plus shield combination as the other conductor. The dielectric medium for the common mode has a higher fraction of air and less polyethylene than that for the difference mode. Also note that the delay times of these two modes at high frequencies are different by 0.11 ns/m out of a nominal value of 5 ns/m. It is difficult to ensure that we have obtained accurate data on this small

value taken as the difference between two large numbers. However, the far-end coupled noise is extremely sensitive to this propagation delay difference. Therefore, the following experiment was performed to arrive at a more accurate value.

One end of a 123-meter cable had the solid blue wire connected to a pulse generator with a fast transition time (less than 2 ns). The orange pair plus shield combination was used as the ground return reference. The blue stripe wire was connected with 50 ohms to the reference conductor. The signal was observed on the far end of both the driven and coupled lines, both terminated with 50 ohms to the reference. The results are shown in Fig. 10, where the output voltages on the driven line and the coupled line are plotted as a function of time. The drastic rise time deterioration observed at the far ends is due to the resistive and skin effect losses. Note that the signal on both lines initially rises together. This indicates that the com-

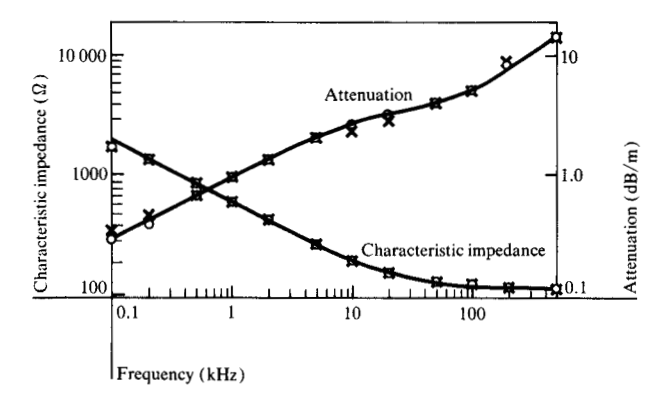


Figure 9 Measured twisted pair attenuation constant and characteristic impedance magnitude as compared to the results derived from difference mode measurements of coupled lines: O—single twisted pair; ×—difference mode of coupled lines.

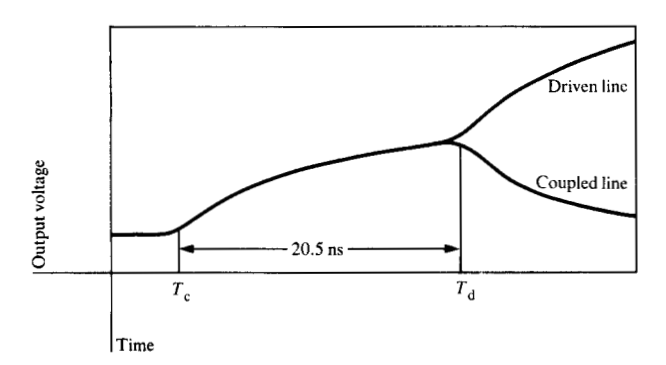


Figure 10 Fast pulse response to determine propagation delay difference for the two decoupled modes. Time T_c is start of common mode; time T_d is start of differential mode.

mon mode is the fast one, consistent with Table 4(b). The difference mode arrives 20.5 ns later, when the signal on the driven line rises again, and that on the coupled line starts to fall. Therefore, the delay time difference between the fast common mode and the slow difference mode is 0.167 ns/m. It is 50% higher than the 0.11 ns/m

On the basis of the information in Table 4, plus the 0.167-ns/m fine adjustment to the high-frequency limit of the common mode and difference mode delay time, we

shown in Table 4(b). But the error is only 1.1% of the 5-

ns/m nominal value, well within measurement accuracy.

Table 5 Coupled transmission line par

Resistance (Ω/km)						
Freq. (kHz)	R11	R12	R22			
0.1	64.06	12.83	64.06			
0.2	64.11	12.36	64.11			
0.5	63.89	12.12	63.89			
1	63.97	12.13	63.97			
	64.01	12.19	64.01			
2 5	63.93	12.26	63.93			
10	64.90	12.45	64.90			
20	68.29	13.25	68.29			
50	77.93	17.36	77.93			
100	101.47	23.59	101.47			
200	125.72	26.09	125.72			

	Capacitance	(μF/km)	
Freq. (kHz)	Ċ11	C12	C22
0.1	0.0862	-0.0140	0.0862
0.2	0.0713	-0.0116	0.0713
0.5	0.0726	-0.0118	0.0726
1	0.0732	-0.0119	0.0732
2	0.0740	-0.0121	0.0740
5	0.0745	-0.0127	0.0745
10	0.0750	-0.0141	0.0750
20	0.0752	-0.0159	0.0752
50	0.0756	-0.0140	0.0756
100	0.0754	-0.0153	0.0754
200	0.0768	-0.0147	0.0768
500	0.0768	-0.0142	0.0768
1000	0.0766	-0.0146	0.0766

Inductance (μH/km)						
Freq. (kHz)	L11	L12	L.22			
2	510.5	99.5	510.5			
5	498.0	98.3	498.0			
10	492.0	96.4	492.0			
20	477.7	94.3	477.7			
50	451.1	81.8	451.1			
100	435.4	81.8	435.4			
200	402.2	68.8	402.2			
500	360.1	58.8	360.1			
1000	340.9	58.0	340.9			

established all ratios of polynomials needed using AS-TAP-compatible routines. The low-frequency limits of R_{11} , R_{12} , and R_{22} were needed only for ASTAP dc initial conditions. From then on, we were ready to perform any dc, transient, and frequency domain simulation of these coupled lines connected with any nonlinear circuits acceptable to ASTAP.

Transient measurements of the 123-meter cable with the same set-up as used to obtain Fig. 10 were repeated, with input signal rise time increased to about 200 ns. The signals at all four nodes (both near and far ends of both

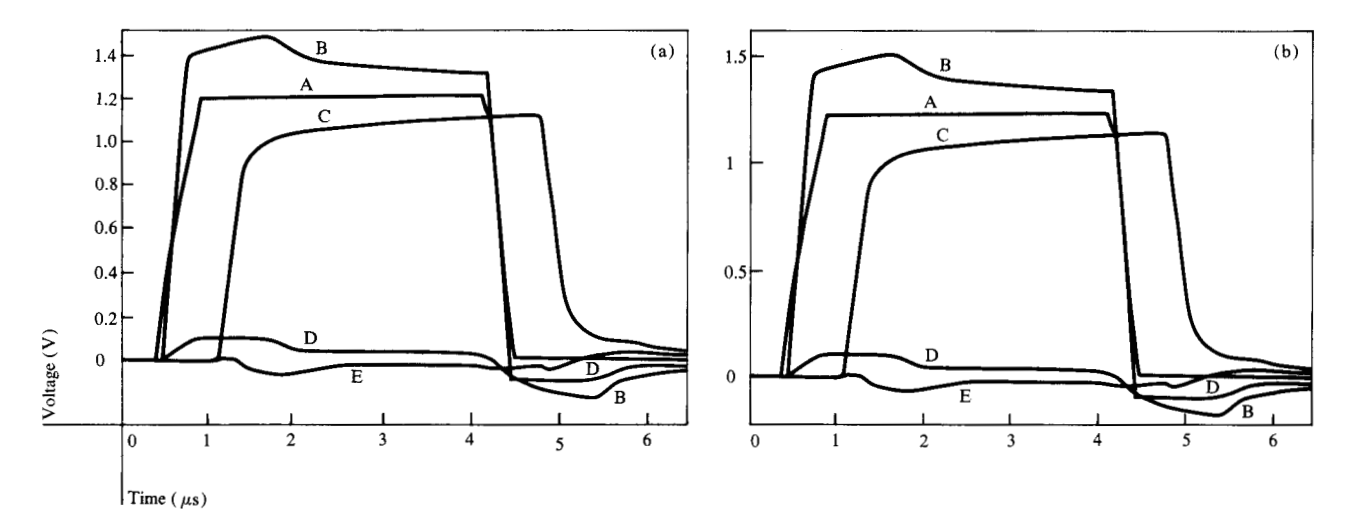


Figure 11 (a) Drive signal from a 50- Ω generator with a 50- Ω load, and measured cable response to the same drive signal when the 50- Ω load is replaced by the coupled lines. Curve A, drive signal; curve B, input to driven line; curve C, output; curve D, near-end coupled noise, and curve E, far-end coupled noise. (b) Predicted coupled line response for the same conditions as (a).

driven and coupled lines) were monitored using a high-impedance probe. The results are shown in Fig. 11(a). The same circuit was simulated, and the results are shown in Fig. 11(b). Also shown in Figs. 11(a) and (b) is the drive signal when a 50-ohm load instead of the cable is connected to the pulse generator. The difference between measurements and simulation is extremely small. Note that the frequency-dependent input admittance, together with the attenuated reflection from the far end, has substantially distorted the driven line near-end waveform, which is quite different from that expected for lossless coupled lines.

In the above ASTAP simulation of two symmetrical coupled lossy lines, we used seven poles and five zeros for both mode 1 and mode 2 attenuation curves; 10 poles and 10 zeros for entries in the characteristic admittance matrices. The total simulation time over the 7-ms duration was 35 s CPU time using an IBM System/370 Model 168 computer.

Note that for this simple example of two symmetrical lines, the eigenvector matrix turns out to be independent of frequency. This, however, is not a restriction of the method discussed in this paper. An analysis of three coupled lines (four conductors) was performed based on a calculated capacitance matrix [34] and a calculated complex impedance matrix [35]. The latter was a function of frequency. The 3×3 eigenvector matrix **P**, as defined in Eq. (5), had five distinct entries which were functions of frequency. Each entry can be approximated by a ratio of

two polynomials. We also observed that the decoupled modes came out of the numerical calculation in a different order at different frequencies in the range of interest.

For the simulation technique described in the paper to work properly, we had to keep track of each of the decoupled modes throughout the frequency range of interest. It was found that the inner product of the two normalized eigenvectors associated with the same decoupled mode at two frequencies within one decade had a magnitude very close to unity. On the other hand, the inner product of the two normalized eigenvectors associated with different decoupled modes had a magnitude much less than unity. Using the inner product of eigenvectors at adjacent frequencies for the tracking of different decoupled modes along the frequency axis proved to work quite well for this exercise involving the four conductor configurations. It is expected that this tracking technique will work for coupled lines having more conductors. If it is necessary, we can progress on the frequency axis in smaller frequency increments to guarantee proper tracking.

The above exercise on the four conductor configurations pointed out that it was possible to have accurate simulation of the transient behavior of coupled transmission lines that had not been built yet.

To show the validity of the polynomial approximations used for transient analysis, we implemented Eq. (8) in the frequency domain analysis portion of ASTAP. The input

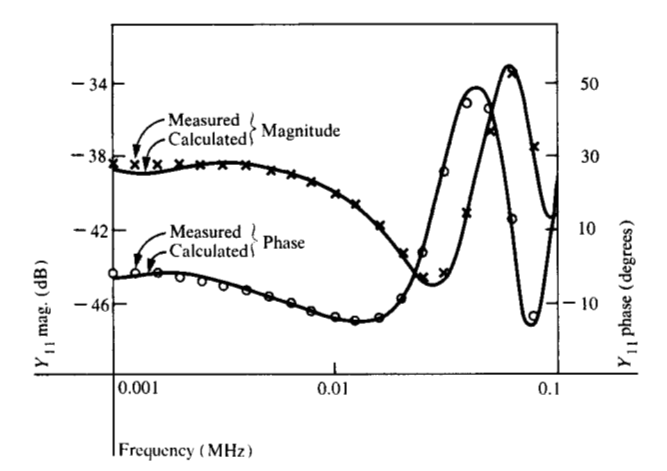


Figure 12 Comparison of measured and calculated Y_{11} magnitude and phase.

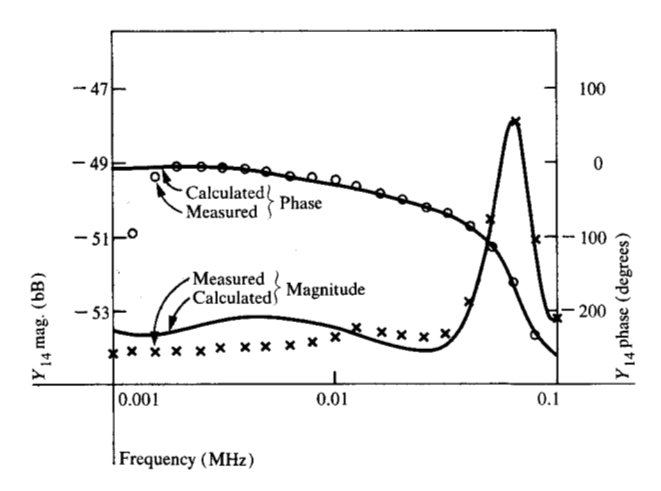


Figure 13 Comparison of measured and calculated Y_{14} magnitude and phase.

to the subroutines that solve Eq. (8) is the same set of polynomial approximations used to obtain the transient simulation model. The short-circuit admittance matrix of the 2n-port network obtained from ASTAP simulation was compared to that obtained from the insertion loss measurements.

The Y_{11} comparison shown in Fig. 12 showed very good agreement in magnitude and phase. The Y_{14} entry, which was the transadmittance from the near end of line one to the far end of line two, turned out to be the one with the worst agreement between simulated and measured values of the eight different Y_{2n} and Z_{2n} parameters. The Y_{14} comparison is shown in Fig. 13. Note that (a) the input data

used to generate the \mathbf{Y}_0 and Γ matrices were the averages of both the open- and short-circuit insertion loss measurements for all possible 1-port and 2-port configurations; (b) the polynomials representing \mathbf{Y}_0 and $\exp{(-\Gamma x)}$ are approximations to the actual curves. The magnitude of Y_{14} is about 10 dB lower than that of Y_{11} . Therefore, the Y_{14} comparison was more prone to measurement and approximation errors.

Conclusions

The (n+1)-conductor coupled transmission lines can be characterized as a 2n-port network using insertion loss measurements in the low-frequency range. The 2n-port network parameters, \mathbf{Y}_{2n} and \mathbf{Z}_{2n} matrices, can be used to derive the coupled line characteristic admittance matrix \mathbf{Y}_0 and propagation matrix $\mathbf{\Gamma}$, both being $n \times n$ matrices. The frequency-dependent transmission line parameters, the \mathbf{R} , \mathbf{L} , \mathbf{G} , and \mathbf{C} matrices, can then be calculated from the \mathbf{Y}_0 and $\mathbf{\Gamma}$ matrices throughout the frequency range of interest. The good agreement of \mathbf{R} , \mathbf{L} , and \mathbf{C} values between the single twisted pair measurements and the difference mode data from the two coupled line measurements demonstrates the validity of this characterization technique.

Taking every entry in the frequency-dependent Y_0 , P, $\exp (-\gamma d)$, and \mathbf{P}^{-1} matrices of the coupled lines as an operator on the line voltage state variable, a transient simulation technique has been developed. It is applicable to the general case of uniform cross-section, multipleconductor transmission lines. They may be imbedded in either homogeneous or inhomogeneous media. They can be connected with linear and/or nonlinear circuits. The simulation results have been compared with the transient measurements of the AWG22 twisted pair and a cable having two coupled lines. The excellent agreement of signal attenuation and waveform distortion substantiates this transient simulation technique. The same input data on transmission line characteristics used for the transient simulation can also be used for the frequency domain simulation.

Acknowledgments

We greatly appreciate help from D. Taylor in the use of the network analyzer. We are also grateful to A. Widman for the "eye pattern" measurement data, and to C. J. Chan for the cable samples used in this paper. We are indebted to W. T. Weeks for many helpful discussions.

Appendix A: Assumptions related to transmission line matrices

These assumptions apply to Z and Y matrices and other related matrices associated with the coupled transmission lines.

1. Any complex symmetrical matrix A, encountered in the transmission line studies, is assumed to be diagonalizable. That is.

$$\mathbf{A} = \mathbf{S}_{\mathbf{A}} \mathbf{\lambda}_{\mathbf{A}} \mathbf{S}_{\mathbf{A}}^{-1} \,,$$

where λ_A is a diagonal matrix. S_A is the eigenvector matrix [28]. Note that each diagonal element, $(\lambda_A)_k$, has two square roots. We shall take the root such that $\text{Re }\{(\lambda_A^{1/2})_k\} \geq 0$. Then define

$$A^{1/2} \equiv S_A \lambda_A^{1/2} S_A^{-1} .$$

It can be proved that $A^{1/2}$ is also symmetrical.

2. Define C = AB, where A and B are complex symmetrical matrices encountered in the transmission line studies. We have assumed that C is diagonalizable. That is,

$$\mathbf{C} = \mathbf{S}_{\mathbf{C}} \mathbf{\lambda}_{\mathbf{C}} \mathbf{S}_{\mathbf{C}}^{-1} .$$

Then

$$\mathbf{C}^{1/2} \equiv \mathbf{S}_C \lambda_C^{1/2} \mathbf{S}_C^{-1} \text{ exists.}$$

Note that $\operatorname{Re} \{(\lambda_{C}^{1/2})_{k}\} \geq 0$ is the root being taken.

Since we are primarily interested in numerical solutions, we shall make small perturbations to the main diagonal elements of A and C matrices in assumptions (1) and (2) to remove the degeneracy in the eigenvalues λ_A and λ_C . Variations by a set of random numbers around 10^{-4} of the magnitude of the main diagonal elements are reasonable perturbations to make with negligible errors in the eigenvalues. With the distinct eigenvalues, the diagonalization of A and C matrices can be ensured.

The existence of Γ in Eq. (5) is implied by assumption (2). We shall prove that Y_0 in Eq. (6) is symmetrical. From assumption (2), we have

$$\mathbf{ZY} = \mathbf{P} \boldsymbol{\gamma}^2 \mathbf{P}^{-1} \,, \tag{A1}$$

$$\Gamma = \mathbf{P} \gamma \mathbf{P}^{-1} = (\mathbf{Z} \mathbf{Y})^{1/2} \,, \tag{A2}$$

where **P** is the eigenvector matrix of **ZY**, and γ is a diagonal matrix having positive real parts.

From Eq. (A1), we have

$$\gamma^{2} = \mathbf{P}^{-1}(\mathbf{Z}\mathbf{Y})\mathbf{P} = \mathbf{P}^{-1}\mathbf{Z}^{1/2}(\mathbf{Z}^{1/2}\mathbf{Y}\mathbf{Z}^{1/2})\mathbf{Z}^{-1/2}\mathbf{P},$$

$$= (\mathbf{Z}^{-1/2}\mathbf{P})^{-1}(\mathbf{Z}^{1/2}\mathbf{Y}\mathbf{Z}^{1/2})(\mathbf{Z}^{-1/2}\mathbf{P}). \tag{A3}$$

Note that for matrix X = ABA, where A and B are complex symmetrical matrices, one can prove that $X^T = X$. That is, X is symmetrical. On the basis of assumption (1), we know that $Z^{1/2}$ exists and is symmetrical. Therefore, $Z^{1/2}YZ^{1/2}$ is symmetrical. From Eq. (A3), we have

$$(\mathbf{Z}^{1/2}\mathbf{Y}\mathbf{Z}^{1/2})^{1/2} = (\mathbf{Z}^{-1/2}\mathbf{P})\gamma(\mathbf{Z}^{-1/2}\mathbf{P})^{-1} = \mathbf{Z}^{-1/2}(\mathbf{P}\gamma\mathbf{P}^{-1})\mathbf{Z}^{1/2}$$

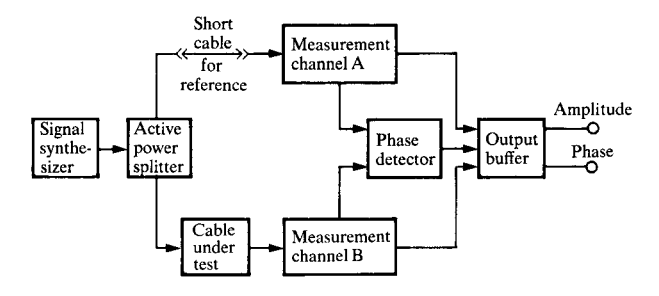


Figure B1 Insertion loss measurement block-diagram.

From the above equation and Eq. (A2), we have

$$\Gamma = \mathbf{P} \mathbf{v} \mathbf{P}^{-1} = \mathbf{Z}^{1/2} (\mathbf{Z}^{1/2} \mathbf{Y} \mathbf{Z}^{1/2})^{1/2} \mathbf{Z}^{-1/2}$$

From the above equation and Eq. (6), we have

$$\mathbf{Y}_{o} = \mathbf{Z}^{-1} \mathbf{\Gamma} = \mathbf{Z}^{-1/2} (\mathbf{Z}^{1/2} \mathbf{Y} \mathbf{Z}^{1/2})^{1/2} \mathbf{Z}^{-1/2}$$
 (A4)

Note that $\mathbf{Z}^{1/2}$ and $(\mathbf{Z}^{1/2}\mathbf{Y}\mathbf{Z}^{1/2})^{1/2}$ are symmetrical matrices. Therefore, \mathbf{Y}_0 is symmetrical, which we set out to prove.

Appendix B: Y_{2n} and Z_{2n} from insertion loss measurements

A 2*n*-port network can be described by its short-circuit admittance matrix as follows:

$$Y_{11}V_1 + Y_{12}V_2 + \cdots + Y_{1,2n}V_{2n} = I_1,$$
.

$$Y_{2n,1}V_1 + Y_{2n,2}V_2 + \cdots + Y_{2n,2n}V_{2n} = I_{2n}$$
 (B1)

If we short-circuit all 2n ports except port p, the 2n-port network becomes a one-port network, having Y_{pp} as its input admittance. It can be measured using the HP3042 network analyzer, which has a block diagram shown in Fig. B1. Channel A is connected with a short cable for reference purposes, while a one-port network having input admittance of Y_{pp} is inserted in the connection to channel B. We then have the situation illustrated in Fig. B2. Therefore,

$$(V_2/V_0)_A = 0.5,$$

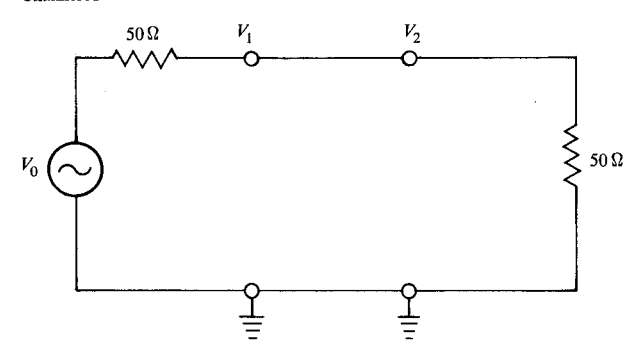
$$(V_2/V_0)_{\rm B} = \frac{Y_{pp}}{2Y_{pp} + G_0} \ .$$

Then the insertion loss is

$$\frac{(V_2/V_0)_{\rm B}}{(V_2/V_0)_{\rm A}} = \frac{2Y_{pp}}{2Y_{pp} + G_0} \equiv \frac{1}{a} ;$$

39





Channel B

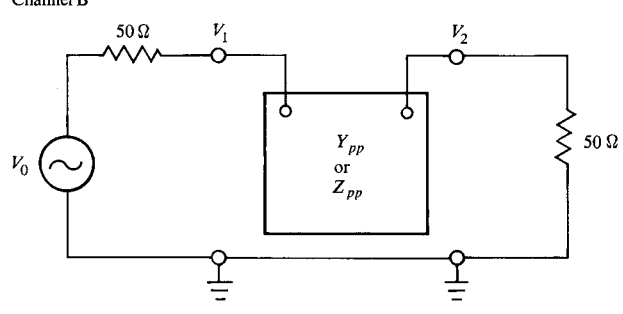
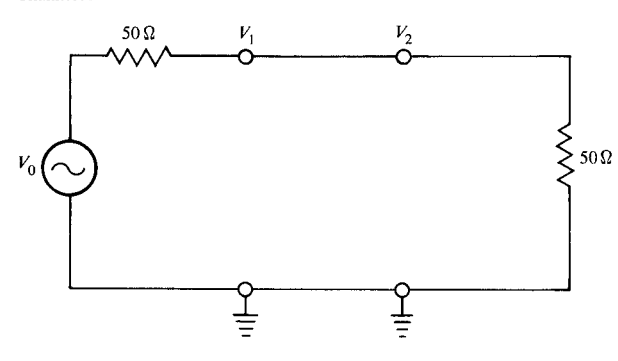


Figure B2 One-port insertion loss measurement set-up.

Channel A



Channel B

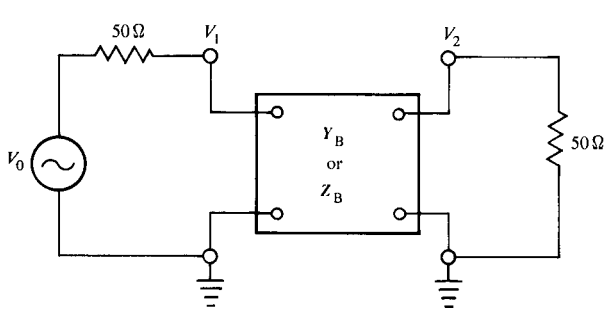


Figure B3 Two-port insertion loss measurement set-up:

$$\mathbf{Y}_{\mathbf{B}} = \begin{bmatrix} Y_{pp} & Y_{pq} \\ Y_{pq} & Y_{qq} \end{bmatrix},$$

$$\mathbf{Z}_{\mathrm{B}} = \begin{bmatrix} Z_{pp} & Z_{pq} \\ Z_{pq} & Z_{qq} \end{bmatrix}.$$

therefore,

$$Y_{pp} = G_0/2(a-1). (B2)$$

We may repeat the above measurement for all 2n ports to derive Y_{kk} , $k = 1, \dots, 2n$.

If we short-circuit all 2n ports except port-p and port-q, Eq. (B1) becomes

$$\begin{split} Y_{pp}V_p + V_{pq}V_q &= I_p \,, \\ Y_{pq}V_p + Y_{qq}V_q &= I_q \,. \end{split} \tag{B3}$$

We may treat this 2n-port network as a two-port network. When it is inserted in the connection to Channel B of the network analyzer, the insertion loss shown in Fig. B3 can be proved to be

$$\frac{(V_2/V_0)_{\rm B}}{(V_2/V_0)_{\rm A}} = \frac{-2Y_{pq}}{(G_0 + Y_{pp})(G_0 + Y_{qq}) - Y_{pq}^2} \equiv \frac{1}{b} \ ; \label{eq:constraint}$$

therefore,

$$Y_{pq} = b - \sqrt{b^2 + (G_0 + Y_{pp})(G_0 + Y_{qq})}$$
 (B4)

We may repeat the above measurement to exhaust all two-port combinations. Then the complete Y_{2n} matrix can be established. Similarly, we may describe the 2n-port network by its open-circuit impedance matrix, and perform the open-circuit one-port and two-port insertion loss measurements. It can be shown that the two-port insertion loss can be expressed as a function of the open-circuit impedance matrix elements as follows:

$$\frac{(V_2/V_0)_{\rm B}}{(V_2/V_0)_{\rm A}} = \frac{2Z_{pq}}{(R_0 + Z_{pp})(R_0 + Z_{qq}) - Z_{pq}^2} \equiv \frac{1}{c} \; ; \label{eq:constraint}$$

therefore,

$$Z_{pq} = -c + \sqrt{c^2 + (R_0 + Z_{pp})(R_0 + Z_{qq})}$$
, (B5)

where Z_{pp} , $p=1,\cdots,2n$, can be obtained from the oneport open-circuit insertion loss measurements. By repeating all combinations of one-port and two-port measurements, we can establish the complete \mathbf{Z}_{2n} matrix.

Note that for passive networks like transmission lines, the \mathbf{Y}_{2n} and \mathbf{Z}_{2n} matrices are symmetrical. Because of measurement accuracy limitations, we may obtain small deviations from symmetry. We take the arithmetic average as follows to ensure symmetry:

$$\mathbf{Y}_{2n} = \frac{1}{2} \left[(\mathbf{Y}_{2n}^{\text{meas}}) + (\mathbf{Y}_{2n}^{\text{meas}})^T \right],$$

$$\mathbf{Z}_{2n} = \frac{1}{2} \left[(\mathbf{Z}_{2n}^{\text{meas}}) + (\mathbf{Z}_{2n}^{\text{meas}})^T \right].$$

40

References and note

- F. H. Branin, Jr., "Transient Analysis of Lossless Transmission Lines," Proc. IEEE 55, 2012 (1967).
- H. Amemiya, "Time Domain Analysis of Multiple Parallel Transmission Lines," RCA Rev. 28, 241 (1967).
- 3. F. Y. Chang, "Transient Analysis of Lossless Coupled Transmission Lines in a Non-homogeneous Dielectric Medium," *IEEE Trans. Microwave Theory Tech.* MTT-18, 616 (1970).
- C. W. Ho, "Theory and Computer-aided Analysis of Loss-less Transmission Lines," IBM J. Res. Develop. 17, 249 (1973).
- K. D. Marx, "Propagation Modes, Equivalent Circuits, and Characteristic Termination for Multiconductor Transmission Lines with Inhomogeneous Dielectrics," *IEEE Trans. Microwave Theory Tech.* MTT-21, 450 (1973).
 H. W. Dommel, "Digital Computer Solutions of Electro-
- H. W. Dommel, "Digital Computer Solutions of Electromagnetic Transients in Single and Multiphase Networks," IEEE Trans. Power App. Syst. PAS-88, 388 (1969).
- 7. A. J. Gruodis, "Transient Analysis of Uniform Resistive Transmission Lines in a Homogeneous Medium," *IBM J. Res. Develop.* 23, 675 (1979).
- 8. R. E. Matick, Transmission Lines for Digital and Communication Networks, McGraw-Hill Book Co., Inc., New York, 1969.
- 9. V. Belevitch, "Theory of the Proximity Effect in Multiconductor Cables," *Philips Rev.* 32, 16 (1977).
- G. S. Eager, Jr., L. Jachimowicz, I. Kolodny, and D. E. Robinson, "Transmission Properties of Polyethylene-Insulated Telephone Cables at Voice and Carrier Frequencies," *IEEE Trans. Commun. Electron.* 78, 618 (1959).
- 11. T. A. Lenahan, "Experimental Test of Propagation—Parameter Calculations for Shielded Balanced Pair Cables," *Bell Syst. Tech. J.* **56**, 627 (1977).
- A. K. Agrawal, K.-M. Lee, L. D. Scott, and H. M. Fowles, "Experimental Characterization of Multiconductor Transmission Lines in Frequency Domain," *IEEE Trans. Electromagnet. Compat.* EMC-21, 20 (1979).
- L. M. Wedepohl, "Application of Matrix Methods to the Solution of Traveling-Wave Phenomena in Polyphase Systems," Proc. IEE 110, 220 (1963).
- 14. H. Guckel and Y. Y. Sun, "Uniform Multimode Transmission Lines," *IEEE Trans. Microwave Theory Tech.* MTT-20, 412 (1972).
- 15. C. R. Paul, "On Uniform Mode Transmission Lines," *IEEE Trans. Microwave Theory Tech.* MTT-21, 556 (1973).
- C. R. Paul, "Useful Matrix Chain Parameters Identities for the Analysis of Multiconductor Transmission Lines," *IEEE Trans. Microwave Theory Tech.* MTT-23, 756 (1975).
- 17. J. R. Carson, "Wave Propagation in Overhead Wires with Ground Return," Bell Syst. Tech. J. 5, 539 (1926).
- L. M. Wedepohl and S. E. T. Mohamed, "Multiconductor Transmission Lines—Theory of Natural Modes and Fourier Integral Applied to Transient Analysis," Proc. IEEE 116, 1553 (1969).
- A. Budner, "Introduction of Frequency-Dependent Line Parameters into an Electromagnetic Transient Program," IEEE Trans. Power App. Syst. PAS-89, 88 (1970).
- J. K. Snelson, "Propagation of Traveling Waves on Transmission Lines—Frequency Dependent Parameters," IEEE Trans. Power App. Syst. PAS-91, 85 (1972).

- 21. W. S. Meyer and H. W. Dommel, "Numerical Modeling of Frequency-Dependent Transmission Line Parameters in an Electromagnetic Transient Program," *IEEE Trans. Power App. Syst.* PAS-93, 1401 (1974).
- D. M. Triezenberg, "An Efficient State Variable Transmission Line Model," *IEEE Trans. Power App. Syst.* PAS-98, 484 (1979).
- 23. G. L. Wilson and K. A. Schmidt, "Transmission Line Models for Switching Studies: Design Criteria, Part II. Selection of Section Length, Model Design and Tests," *IEEE Trans. Power App. Syst.* PAS-93, 389 (1974).
- 24. S. J. Garrett, "Transmission Line Models for Transient Analysis," *Proc. 11th Design Automation Conference*, Denver, CO, June 17-19, 1974, p. 209.
- S. P. Madyiwa, IBM Data Systems Division, Poughkeepsie, NY, private communication.
- F. Briglez, "Design of RL Networks Beyond 100 MHz," IEEE Trans. Circuits Syst. CAS-23, 650 (1976).
- 27. Advanced Statistical Analysis Program (ASTAP), Program Reference Manual, Pub. No. SH20-1118-0, IBM Corporation, Data Processing Division, White Plains, NY 10604.
- F. G. Gantmacher, The Theory of Matrices, Vol. 1, Chelsea Publishing Co., New York, 1959.
- L. M. Wedepohl, "Electrical Characteristics of Polyphase Transmission System with Special Reference to Boundary-Value Calculation at Power Line Carrier Frequencies," Proc. IEE 112, 2103 (1965).
- J. C. Bowers and S. R. Sedore, SCEPTRE, A Computer Program for Circuit and Systems Analysis, Prentice-Hall, Inc., Englewood Cliffs, NJ, 1971.
- 31. P. M. Wilberg, State Space and Linear Systems, McGraw-Hill Book Co., Inc., New York, 1974.
- The ASTAP runs quoted in this paper have used many subroutines added to that of Reference 27.
- R. W. Lucky, J. Salz, and E. J. Weldon, Jr., Principles of Data Communications, McGraw-Hill Book Co., Inc., New York, 1968, p. 61.
- W. T. Weeks, "Calculation of Coefficients of Capacitance of Multiconductor Transmission Lines in the Presence of a Dielectric Interface," *IEEE Trans. Microwave Theory Tech.* MTT-18, 35 (1970).
- 35. W. T. Weeks, L. L. Wu, M. F. McAllister, and A. Singh, "Resistive and Inductive Skin Effect in Rectangular Conductors," *IBM J. Res. Develop.* 23, 652 (1979).

Received May 23, 1980; revised August 14, 1980

The authors are located at the IBM Data Systems Division laboratory, East Fishkill (Hopewell Junction), New York 12533.